

Contactless Microwave Characterization of Encapsulated Graphene p - n Junctions

V. Ranjan,^{1,*} S. Zihlmann,¹ P. Makk,¹ K. Watanabe,² T. Taniguchi,² and C. Schöenberger^{1,†}

¹Department of Physics, University of Basel, Klingelbergstrasse 82, 4056 Basel, Switzerland

²National Institute for Material Science, 1-1 Namiki, Tsukuba, 305-0044, Japan

(Received 7 February 2017; revised manuscript received 10 April 2017; published 24 May 2017)

Accessing intrinsic properties of a graphene device can be hindered by the influence of contact electrodes. Here, we capacitively couple graphene devices to superconducting resonant circuits and observe clear changes in the resonance frequency and widths originating from the internal charge dynamics of graphene. This allows us to extract the density of states and charge relaxation resistance in graphene p - n junctions without the need for electrical contacts. The presented characterization paves a fast, sensitive, and noninvasive measurement of graphene nanocircuits.

DOI: 10.1103/PhysRevApplied.7.054015

I. INTRODUCTION

In the past decade, extensive studies on graphene have unfolded interesting physics of Dirac particles on chip [1–4]. Up to now the main technique to study the electronic properties of graphene has been a low-frequency lock-in technique where electrical contacts are needed for conductance measurements. The key drawbacks of contact electrodes are highly doped regions in the vicinity of the contacts resulting in unwanted p - n junctions [5] and scattering [6] of charge carriers. In addition, added resist residues from lithography can degrade the metal-graphene interfacial properties [7] or even the overall device quality. An important example of this is graphene spintronics [8], where device performance is often limited by the contacts, which cause spin relaxation and decrease of the spin lifetime [9–12]. Therefore, contactless characterization such as microwave absorption [13] and microwave-impedance microscopy [14] can open up new ways to probe inherent properties of the studied system. In the past, other contactless schemes such as terahertz spectroscopy [15,16] and dielectric force microscopy [17] have been employed to study the carrier dynamics in graphene. In contrast to the former, microwave response utilized in this work precludes any interband or intraband transitions allowing studies of carriers at the Fermi level. More importantly, our devices and readout circuits, stub tuners [18], can be easily integrated on chip and the resonant response can be exploited to extract both the quantum capacitance and the charge relaxation resistance with a single measurement even in the absence of electrical contacts.

We have used high-mobility graphene encapsulated in hexagonal boron nitride [19,20], which separates the graphene from external perturbations and allows local gating of the graphene flake. By forming a p - n junction the internal charge dynamics of the graphene circuit can be probed and

by analyzing the microwave response of the circuit the charge relaxation resistance as well as the quantum capacitance can be inferred. Our measurements allow us to study p - n junctions in a contactless way, which are potential building blocks of electron optical devices [21–27].

II. DEVICE LAYOUT

Figure 1 shows the layout of a typical device. The stub-tuner circuit is based on two transmission lines TL_1 and

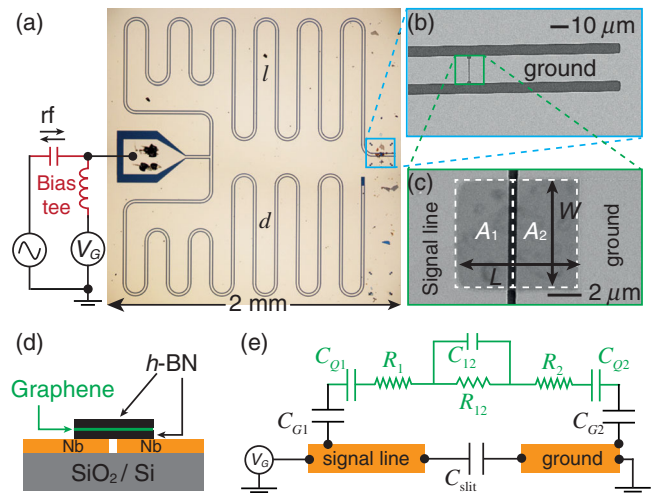


FIG. 1. Sample layout. (a) An optical picture of the stub tuner with arm lengths l and d . Central conductor and gap widths of the transmission lines are 15 and 6 μm , respectively. Light areas show the Nb film and darker areas are exposed SiO_2 substrate after Nb is etched away. (b) An SEM image near the l end showing a narrow slit between the signal line and the ground plane. (c) An SEM image of a h -BN/graphene/ h -BN stack for device B placed over the slit. Areas A_1 and A_2 correspond to two parts of graphene lying on the signal line and the ground plane. (d) A cross section schematic of the device near the slit. (e) An equivalent circuit with lumped capacitance and resistance elements.

*vishal.ranjan@unibas.ch

†Christian.Schoenberger@unibas.ch

TL₂ of lengths l and d , respectively, each close to $\lambda/4$ [18]. The operation of the circuit can be understood in a simple analogy to optics. The T junction near the launcher acts like a beam splitter. The incident wave splits into the two arms of the circuit and gets reflected at the open end and the device end, and then interferes back at the junction providing the resonance condition. The circuit is patterned using a 100-nm-thick niobium film by e -beam lithography and subsequent dry etching with Ar/Cl₂. To minimize microwave losses, high resistive silicon substrates (with 170 nm of SiO₂ on top) are used. The signal line of TL₁ features a slit of width ~ 450 nm near the end before terminating in the ground plane, as shown in Figs. 1(b) and 1(c). We place the graphene stack, encapsulated in hexagonal boron nitride (h -BN), over the slit. The h -BN/graphene/ h -BN stack is prepared using the dry transfer method described in Refs. [19,28], and positioned in the middle of the slit such that parts of the flake lie on the signal line and parts on the ground plane. We then etch the stack with SF₆ in a reactive ion etcher to create a well-defined rectangular geometry. Some bubbles resulting from the transfer can also be seen in Fig. 1(c). Raman spectroscopy [29] is used to verify the single-layer nature of the graphene used in this study (see Supplemental Material [30]).

Since there are no evaporated contacts on graphene, the same circuit can be employed for different stack geometries. We first fabricate a device with stack dimensions $W \times L$ of $6.5 \mu\text{m} \times 13 \mu\text{m}$ (device A), where W and L , respectively, denote the width and length of the rectangular graphene. After measurements on device A , the stack is etched into new dimensions of $6.5 \mu\text{m} \times 7.2 \mu\text{m}$ (device B). For both devices, a graphene area of $6.5 \mu\text{m} \times 3.4 \mu\text{m}$ stays on the signal (gate) line, see Fig. 1(c). The graphene sections lying above the ground plane had areas of $6.5 \mu\text{m} \times 9.6 \mu\text{m}$ for device A , and $6.5 \mu\text{m} \times 3.8 \mu\text{m}$ for device B . Device A is hence asymmetric while device B is quasisymmetric around the slit. More importantly, two devices on the same circuit with the same graphene flake but different geometry provide consistency checks. A third symmetric device C of dimensions $5 \mu\text{m} \times 12 \mu\text{m}$ with a separate resonator circuit and a different graphene stack is also measured.

III. MEASUREMENT PRINCIPLE

We extract the graphene properties by measuring the complex reflection coefficient of the stub tuner, which depends on the rf admittance of a load [31]. The reflected part of the rf (radio frequency) probe signal fed into the launcher port of the circuit is measured using a vector network analyzer. To tune the Fermi level of the graphene a dc voltage V_G is also applied to the launcher port with the help of a bias tee, as shown in Fig. 1(a). The gate voltage changes (locally) the carrier density and hence the quantum capacitance. By analyzing the response of the circuit, changes in differential capacitance, related to the quantum capacitance C_Q and in dissipation, related to charge

relaxation resistance R can be extracted. All reflectance measurements are performed at an input power of -110 dBm and at a temperature of 20 mK. The latter is chosen only to have a good quality factor of the resonance response of the superconducting niobium circuits.

To understand the effect of gating, we divide the graphene into two areas denoted by A_1 and A_2 in Fig. 1(c). A gate voltage on the signal line induces charges on the part of the graphene flake above it. Since the total number of charges in the absence of a contact cannot change, charges on one part must be taken from the other. For a pristine graphene with the Fermi level at the charge neutrality point (CNP) without gating, this results in the formation of a p - n junction near the slit at each gate voltage. However, when a finite offset doping is present, an offset voltage has to be applied and the charge neutrality is reached at two different gate voltages, once for each part of graphene. At voltages higher than these offset voltages (in absolute value) a p - n junction is present in the graphene. The charge carrier density changes rapidly close to the slit, but it is constant further away from the slit. Because of different areas A_1 and A_2 , the applied gate voltage results into different charge densities, but equal and opposite total charge on the two sides.

In the transmission line geometry, the rf electric field emerges from the signal plane and terminates on the ground plane. While the field lines are quasiperpendicular to the graphene surface further away from the slit, they become parallel and relatively stronger in magnitude near the slit. The field distribution hence probes both the properties of the bulk graphene (homogeneous charge distribution) and the junction graphene (inhomogeneous charge distribution). For simplicity, we model the graphene as lumped one-dimensional elements of capacitance and resistance as shown in Fig. 1(e). The graphene impedance is then simply given as $Z_G \sim R + 1/(j\omega C)$ with the total series capacitance C and resistance R as

$$\frac{1}{C} = \frac{1}{C_{G1}} + \frac{1}{C_{Q1}} + \frac{1}{C_{G2}} + \frac{1}{C_{Q2}}, \quad (1)$$

$$R = R_1 + R_{12} + R_2, \quad (2)$$

where $\omega = 2\pi f$ the angular frequency. Thus, $C_Q = C_{Q1}C_{Q2}/(C_{Q1} + C_{Q2})$ and $C_G = C_{G1}C_{G2}/(C_{G1} + C_{G2})$ are the total quantum and geometric capacitances of the graphene device. We have assumed that the junction capacitance C_{12} is relatively small so that the junction resistance $R_{12} \ll 1/(\omega C_{12})$. Moreover, we ignore the parallel slit capacitance C_{slit} which is small and gate independent. Together with the load Z_G , the reflectance response Γ of the stub tuner can now be described by $[(Z_{\text{in}} - Z_0)/(Z_{\text{in}} + Z_0)]^2$ where the input impedance Z_{in} is given as [32]

$$Z_{\text{in}} = Z_0 \left(\tanh(\gamma d) + \frac{Z_0 + Z_G \tanh(\gamma l)}{Z_G + Z_0 \tanh(\gamma l)} \right)^{-1}, \quad (3)$$

with $Z_0 \sim 50 \Omega$ the characteristic impedance of the transmission line, $\gamma = \alpha + i\beta$ the propagation constant, α the attenuation constant, $\beta = \sqrt{\epsilon_{\text{eff}}}\omega/c$ the phase constant, ϵ_{eff} the effective dielectric constant, and c the speed of light.

IV. EXPERIMENTAL RESULTS

Figure 2(a) shows a color map of frequency and gate voltage response of the reflected signal for device B. Large frequency shifts at two gate voltages can be observed near $V_G = 0$. These can be identified as points where either part of the graphene flake is driven charge neutral. At higher gate voltages, p - n junctions are formed in between the unipolar regimes. This behavior is observed in all our devices, suggesting the presence of a finite offset doping in the system. From the vertical cuts of the map shown in Fig. 2(b), changes in the resonance depth, resonance width, and resonance frequency are apparent. Naively, a pure

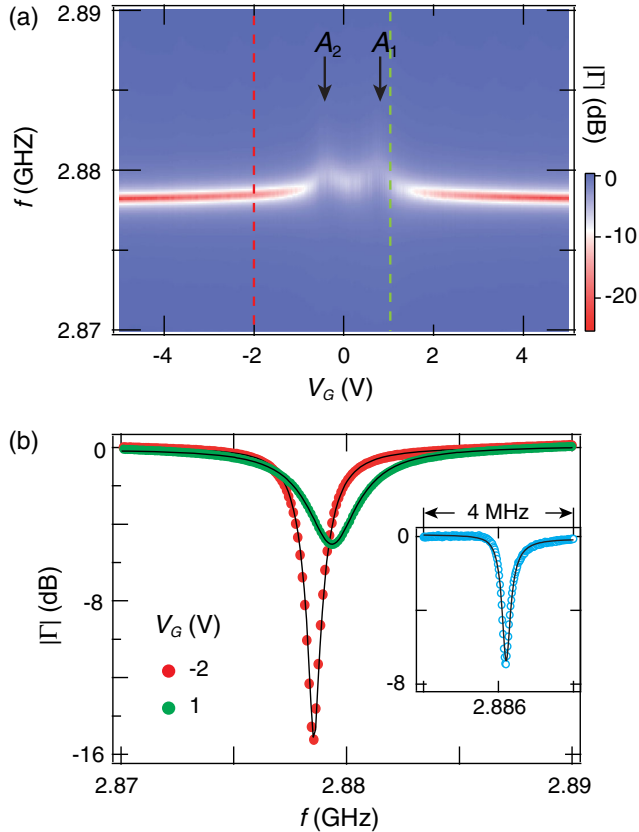


FIG. 2. Reflectance response of the stub tuner. (a) A color map of the measured reflectance power near the resonance frequency versus different gate voltages. Arrows denote the charge neutrality points (CNP) corresponding to respective graphene parts. Its asymmetric separation around the zero voltage is due to inhomogeneous distribution of an average offset doping $\sim 3 \times 10^{11} \text{ cm}^{-2}$ in the system. (b) Main panel: Cuts of the reflectance curves at two different gate voltages with fits to Eq. (3). Inset: The reflectance response of the same device without graphene. The input rf power is -110 dBm , which corresponds to an ac excitation amplitude of $0.7 \mu\text{V}$.

capacitive load should shift the resonance frequency, while a pure resistive load changes dissipation of the system.

To quantitatively extract Z_G , we first need to extract the parameters l , d , α , and ϵ_{eff} from the reflectance measurements of the same circuit without any graphene stack. To this end, we simply ash the graphene stack away using Ar/O₂ plasma. The frequency response of the open circuit is shown in the inset of Fig. 2(b) together with a fit to Eq. (3) with $Z_G = \infty$. We extract $l \approx 10.57 \text{ mm}$ and $d \approx 10.39 \text{ mm}$, $\alpha \approx 0.0025 \text{ m}^{-1}$ and the effective dielectric constant $\epsilon_{\text{eff}} \approx 6.1$. The loss constant corresponds to an internal quality factor of 25 000 which is readily achieved with superconducting Nb circuits. The extracted lengths are within 1% of the designed geometric lengths. Moreover, the resonance frequency of the open stub tuner (2.886 GHz) is larger than the values observed in Fig. 2(a), confirming the capacitive load of our devices. We now fix the extracted parameters from open circuit, and fit the resonance spectra to deduce R and C . As shown in Fig. 2(b), the fitting to Eq. (3) yields $R = 118 \Omega$, $C = 18.2 \text{ fF}$ for $V_G = -2 \text{ V}$ and $R = 328 \Omega$ and $C = 17.2 \text{ fF}$ for $V_G = 1 \text{ V}$. Similar fitting is performed at all gate voltages and deduced C and R are plotted in Figs. 3 and 4.

As shown in Fig. 3, we observe for both devices a double dip feature in the extracted capacitance near $V_G = 0 \text{ V}$ and its saturation at higher voltages. While the dips have similar widths for device B, these are quite different for device A. This again results from the asymmetric gating of the two areas of graphene. To understand the general dependence, we look back at the individual capacitance contributions in Eq. (1). Geometric capacitance C_{Gi} with $i = 1, 2$ is simply given by $C_{Gi} = A_i \epsilon_0 \epsilon_{\text{BN}} / d$, where ϵ_0 is the vacuum permittivity, ϵ_{BN} the dielectric constant, and $d = 21.5 \text{ nm}$ the thickness of the bottom h -BN estimated from AFM measurements. Additionally, the quantum capacitance can be derived from the density of states

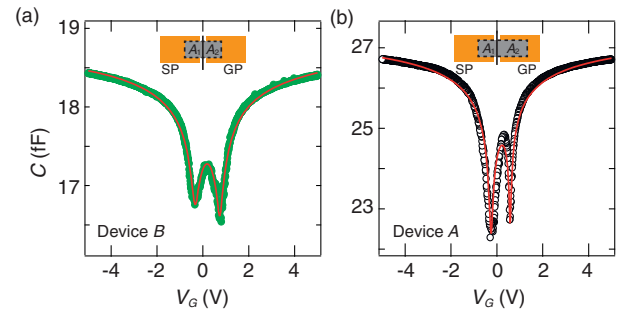


FIG. 3. Quantum capacitance of graphene. (a) The extracted capacitance from the fitting of the reflectance response to Eq. (3) for device B and (b) for device A. Error bars are smaller than the symbol size. Solid lines are the best fits to Eq. (1) showing good agreement with the graphene density of states. Insets: schematics of relative dimensions of graphene flake across the slit. In device B, areas lying on the signal plane (SP) and on the ground plane (GP) are similar, $A_2 \approx A_1$. In contrast for device A, areas $A_2 \approx 2A_1$.

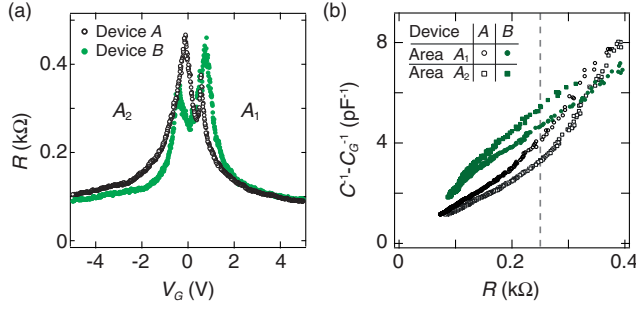


FIG. 4. Dissipation in graphene. (a) The extracted charge relaxation resistance for two devices fabricated on the same *h*-BN/graphene/*h*-BN stack. The same loss constant is used in fitting the reflectance map. (b) Inverse quantum capacitance, obtained by subtracting geometric capacitance from the total extracted capacitance, as a function of the simultaneously extracted charge relaxation resistance.

(DOS) as $C_Q/A = e^2 \text{DOS}$. The resulting dependence of C_Q in graphene with gate voltage V is then explicitly given as [33–36]

$$C_{Qi}(V) = A_i \frac{4e^2}{h v_F} \sqrt{n_i(V) \pi}, \quad (4)$$

with $i = 1, 2$ and v_F the Fermi velocity and h the Planck constant. The gate induced carrier density is $n_i(V) = (V_i - V_i^0) C_{Gi} / (A_i e)$, where V_i^0 accounts for the offset in CNP from zero. Using Eqs. (1) and (4), it can be seen that the C is dominated by the C_G at large gate voltages causing the saturation of the extracted capacitance. The saturation values are different for the two devices because different flake areas yield different C_G . In contrast, near charge neutrality $C_Q \lesssim C_G$, the quantum capacitance starts to dominate. The fact that C does not approach zero can be attributed to the impurity-induced doping $\langle n_{\text{imp},i}^2 \rangle$, with $i = 1, 2$, resulting from charge puddles [37]. To this end, we replace $n_i(V)$ with a total carrier density including this factor $\sqrt{n_i^2(V) + n_{\text{imp},i}^2}$. The knowledge of most of the relevant parameters allows us to fit the capacitance curves with ϵ_{BN} , n_{imp} , and v_F as fitting parameters. This is shown by solid curves in Fig. 3. The excellent fits to Eq. (1) capture both the depth and width near the charge neutrality points and justify the series model of the graphene impedance with C arising from the total graphene area. For device A(B) we extract $\epsilon_{\text{BN}} \approx 4(4)$, $v_F \approx 1.05(0.95) \times 10^6$ m/s and $n_{\text{imp},1} \approx 5(7) \times 10^{10}$ cm $^{-2}$ and $n_{\text{imp},2} \approx 1(6) \times 10^{10}$ cm $^{-2}$. The low impurity carrier concentration is consistent with transport measurements in graphene encapsulated with *h*-BN [37]. In another symmetric device C (see Fig. S2 in the Supplemental Material [30]) with a different circuit and a different stack, the n_{imp} is found to be even lower $\approx 4 \times 10^9$ cm $^{-2}$ and extracted Fermi velocity higher $\approx 1.54 \times 10^6$ m/s. Such renormalization of v_F due to electron-electron interactions at low doping has been

observed both in capacitance [36] and transport measurements [38–40] in homogeneously doped graphene.

We now discuss the real part of the graphene impedance which relates to the dissipation of the microwave resonance. The extracted R for two devices fabricated from the same *h*-BN/graphene/*h*-BN stack (devices A and B) is plotted in Fig. 4(a). Two peaks are visible in the extracted resistances, which are similar to the charge neutrality points in transport measurements. The positions of the peaks correspond to the minima of the extracted capacitance. At large gate voltages where residual impurities play a negligible role, the resistances start to saturate around similar values despite the fact that device A is twice as long as device B. In the absence of contacts, this points to the direction that the resistance is dominated by the *p*-*n* junction at high doping. A similar behavior of R is seen in the device C (see Fig. S2(c) in the Supplemental Material [30]). Close to CNPs, the respective bulk graphene areas also contribute significantly to the resistance. These features are in agreement with the density dependence of the conductivity in the bulk and in the *p*-*n* junction. While the conductivity for the *p*-*n* junction [41] is proportional to $n^{1/4}$, it scales as n or $n^{1/2}$ for bulk graphene depending on the relevant scattering mechanisms [42].

The bulk carrier transport in graphene can be characterized by the diffusion constant D . By knowing both R and C_Q , D can be calculated from the Einstein relation

$$D = (L)^2 / (RC_Q). \quad (5)$$

A complication in our devices arises due to the presence of a *p*-*n* junction which is almost always present. We can, therefore, only get an estimate of D by considering R and C_Q , that are largely arising from only one graphene area A_1 or A_2 . For higher gate voltages, the *p*-*n* junction resistance plays a role, whereas close to the CNPs, both areas contribute to the resistance and the capacitance significantly. The inverse of the quantum capacitance, obtained by subtracting the total geometric contribution C_G from the total extracted C , is now plotted against the simultaneously measured resistance R in Fig. 4(b). We have taken the data points that are strictly on the left (negative V_G) or the right side of CNPs (positive V_G). We extract D at a modest doping marked by the dashed line in Fig. 4(b). Since one cannot separate the contribution of *p*-*n* resistance, by using the total R in Eq. (5), bulk graphene resistance is overestimated and therefore D is underestimated. In graphene areas A_1 lying on signal plane (not changed after etching), we get $D = 0.19(0.21) \times 10^4$ cm 2 /s for device A (B). In contrast, for area A_2 lying on the ground plane, we get $1.2(0.32) \times 10^4$ cm 2 /s. The large differences in D for area A_2 between two devices is consistent with variations in the impurity concentration extracted from the fitting of the capacitance, and could result from the additional etching step of the stack for device B. We, furthermore, estimate an average mean free path of two areas $l_m = 2\langle D \rangle / v_F$ to yield

1.4 (0.5) μm for device A (B), which are in reasonable agreement with values reported in transport measurements.

V. DISCUSSIONS

In summary, we have capacitively coupled encapsulated graphene devices to high quality microwave resonators and observed clear changes in the resonance linewidth and frequency as a response to changes in the gate voltage. We are able to reliably extract geometrical and quantum capacitance in good agreement with the density of states of graphene and simple capacitance models, respectively. Moreover, the charge relaxation resistance can be simultaneously inferred and the diffusion constant can be estimated. The results highlight a fast characterization of graphene without requiring any contacts that could compromise the device quality.

An uncertainty of the given measurements lies in the extracted R due to the loss constant α of the circuit which can vary from one cool down of the device to the next (see Fig. S4 in the Supplemental Material [30]). The α could be, however, accurately determined, without the need for graphene removal and separate cooldown, in the quantum Hall regime where the conductance of the device is known. For this purpose, due to the large magnetic fields, copper resonators [43] have to be fabricated which will also enable measurements at elevated temperatures.

The ability of our circuit to measure quantum capacitance and resistance in a contactless way can, for example, be useful to study band modifications of graphene due to proximity spin orbit effects [44] or due to moiré superlattices [45]. The method can also be useful for other 2D materials, on which an ohmic contact is challenging to obtain and can be easily extended to semiconducting transition metal dichalcogenides and perovskites [3].

ACKNOWLEDGMENTS

This work was funded by the Swiss National Science Foundation, the Swiss Nanoscience Institute, the Swiss NCCR QSIT, the ERC Advanced Investigator Grant QUEST, iSpinText Flag-ERA network, and the EU flagship project graphene. Growth of hexagonal boron nitride crystals was supported by the Elemental Strategy Initiative conducted by the MEXT, Japan and JSPS KAKENHI Grants No. JP26248061, No. JP15K21722, and No. JP25106006. The authors thank Gergő Fülöp for fruitful discussions.

-
- [1] A. H. Castro Neto, F. Guinea, N. M. R. Peres, K. S. Novoselov, and A. K. Geim, The electronic properties of graphene, *Rev. Mod. Phys.* **81**, 109 (2009).
 [2] S. Das Sarma, Shaffique Adam, E. H. Hwang, and Enrico Rossi, Electronic transport in two-dimensional graphene, *Rev. Mod. Phys.* **83**, 407 (2011).

- [3] A. K. Geim and I. V. Grigorieva, Van der Waals heterostructures, *Nature (London)* **499**, 419 (2013).
 [4] Yuan Liu, Nathan O. Weiss, Xidong Duan, Hung-Chieh Cheng, Yu Huang, and Xiangfeng Duan, Van der Waals heterostructures and devices, *Nat. Rev. Mater.* **1**, 16042 (2016).
 [5] G. Giovannetti, P. A. Khomyakov, G. Brocks, V. M. Karpan, J. van den Brink, and P. J. Kelly, Doping Graphene with Metal Contacts, *Phys. Rev. Lett.* **101**, 026803 (2008).
 [6] Antonino La Magna and Ioannis Deretzis, Theoretical study of the role of metallic contacts in probing transport features of pure and defected graphene nanoribbons, *Nanoscale Res. Lett.* **6**, 234 (2011).
 [7] Joshua A. Robinson, Michael LaBella, Mike Zhu, Matt Hollander, Richard Kasarda, Zachary Hughes, Kathleen Trumbull, Randal Cavalero, and David Snyder, Contacting graphene, *Appl. Phys. Lett.* **98**, 053103 (2011).
 [8] Wei Han, Roland K. Kawakami, Martin Gmitra, and Jaroslav Fabian, Graphene spintronics, *Nat. Nanotechnol.* **9**, 794 (2014).
 [9] F. Volmer, M. Drögeler, E. Maynicke, N. von den Driesch, M. L. Boschen, G. Güntherodt, and B. Beschoten, Role of MgO barriers for spin and charge transport in Co/MgO/graphene nonlocal spin-valve devices, *Phys. Rev. B* **88**, 161405 (2013).
 [10] T. Maassen, I. J. Vera-Marun, M. H. D. Guimarães, and B. J. van Wees, Contact-induced spin relaxation in Hanle spin precession measurements, *Phys. Rev. B* **86**, 235408 (2012).
 [11] Gordon Stecklein, Paul A. Crowell, Jing Li, Yoska Anugrah, Qun Su, and Steven J. Koester, Contact-Induced Spin Relaxation in Graphene Nonlocal Spin Valves, *Phys. Rev. Applied* **6**, 054015 (2016).
 [12] Walid Amamou, Zhisheng Lin, Jeremiah van Baren, Serol Turkyilmaz, Jing Shi, and Roland K. Kawakami, Contact induced spin relaxation in graphene spin valves with Al₂O₃ and MgO tunnel barriers, *APL Mater.* **4**, 032503 (2016).
 [13] Jan Obrzut, Caglar Emiroglu, Oleg Kirillov, Yanfei Yang, and Randolph E. Elmquist, Surface conductance of graphene from non-contact resonant cavity, *Measurement* **87**, 146 (2016).
 [14] Y.-T. Cui, B. Wen, E. Y. Ma, G. Diankov, Z. Han, F. Amet, T. Taniguchi, K. Watanabe, D. Goldhaber-Gordon, C. R. Dean, and Z.-X. Shen, Unconventional Correlation between Quantum Hall Transport Quantization and Bulk State Filling in Gated Graphene Devices, *Phys. Rev. Lett.* **117**, 186601 (2016).
 [15] Feng Wang, Yuanbo Zhang, Chuanshan Tian, Caglar Girit, Alex Zettl, Michael Crommie, and Y. Ron Shen, Gate-variable optical transitions in graphene, *Science* **320**, 206 (2008).
 [16] Z. Q. Li, E. A. Henriksen, Z. Jiang, Z. Hao, M. C. Martin, P. Kim, H. L. Stormer, and D. N. Basov, Dirac charge dynamics in graphene by infrared spectroscopy, *Nat. Phys.* **4**, 532 (2008).
 [17] Cristina Gomez-Navarro, Francisco J. Guzman-Vazquez, Julio Gomez-Herrero, Juan J. Saenz, and G. M. Sacha, Fast and non-invasive conductivity determination by the dielectric response of reduced graphene oxide: An electrostatic force microscopy study, *Nanoscale* **4**, 7231 (2012).
 [18] Gabriel Puebla-Hellmann and Andreas Wallraff, Realization of gigahertz-frequency impedance matching circuits for nanoscale devices, *Appl. Phys. Lett.* **101**, 053108 (2012).
 [19] L. Wang, I. Meric, P. Y. Huang, Q. Gao, Y. Gao, H. Tran, T. Taniguchi, K. Watanabe, L. M. Campos, D. A. Muller, J. Guo, P. Kim, J. Hone, K. L. Shepard, and C. R. Dean,

- One-dimensional electrical contact to a two-dimensional material, *Science* **342**, 614 (2013).
- [20] A. V. Kretinin, Y. Cao, J. S. Tu, G. L. Yu, R. Jalil, K. S. Novoselov, S. J. Haigh, A. Gholinia, A. Mishchenko, M. Lozada, T. Georgiou, C. R. Woods, F. Withers, P. Blake, G. Eda, A. Wirsig, C. Hucho, K. Watanabe, T. Taniguchi, A. K. Geim, and R. V. Gorbachev, Electronic properties of graphene encapsulated with different two-dimensional atomic crystals, *Nano Lett.* **14**, 3270 (2014).
- [21] Shaowen Chen, Zheng Han, Mirza M. Elahi, K. M. Masum Habib, Lei Wang, Bo Wen, Yuanda Gao, Takashi Taniguchi, Kenji Watanabe, James Hone, Avik W. Ghosh, and Cory R. Dean, Electron optics with p - n junctions in ballistic graphene, *Science* **353**, 1522 (2016).
- [22] Vadim V. Cheianov, Vladimir Fal'ko, and B. L. Altshuler, The focusing of electron flow and a Veselago lens in graphene p - n junctions, *Science* **315**, 1252 (2007).
- [23] Peter Rickhaus, Romain Maurand, Ming-Hao Liu, Markus Weiss, Klaus Richter, and Christian Schönberger, Ballistic interferences in suspended graphene, *Nat. Commun.* **4**, 2342 (2013).
- [24] Anya L. Grushina, Dong-Keun Ki, and Alberto F. Morpurgo, A ballistic pn junction in suspended graphene with split bottom gates, *Appl. Phys. Lett.* **102**, 223102 (2013).
- [25] Peter Rickhaus, Peter Makk, Hao Liu Ming, Klaus Richter, and Christian Schönberger, Gate tuneable beamsplitter in ballistic graphene, *Appl. Phys. Lett.* **107**, 251901 (2015).
- [26] Peter Rickhaus, Ming-Hao Liu, Péter Makk, Romain Maurand, Samuel Hess, Simon Zihlmann, Markus Weiss, Klaus Richter, and Christian Schönberger, Guiding of electrons in a few-mode ballistic graphene channel, *Nano Lett.* **15**, 5819 (2015).
- [27] Gil-Ho Lee, Geon-Hyoung Park, and Hu-Jong Lee, Observation of negative refraction of Dirac fermions in graphene, *Nat. Phys.* **11**, 925 (2015).
- [28] P. J. Zomer, M. H. D. Guimaraes, J. C. Brant, N. Tombros, and B. J. van Wees, Fast pick up technique for high quality heterostructures of bilayer graphene and hexagonal boron nitride, *Appl. Phys. Lett.* **105**, 013101 (2014).
- [29] Andrea C. Ferrari and Denis M. Basko, Raman spectroscopy as a versatile tool for studying the properties of graphene, *Nat. Nanotechnol.* **8**, 235 (2013).
- [30] See Supplemental Material at <http://link.aps.org/supplemental/10.1103/PhysRevApplied.7.054015> for the Raman spectroscopy of device C, results of a third device C, and a discussion on the extraction of the parameters with different circuit losses.
- [31] V. Ranjan, G. Puebla-Hellmann, M. Jung, T. Hasler, A. Nunnenkamp, M. Muoth, C. Hierold, A. Wallraff, and C. Schönberger, Clean carbon nanotubes coupled to superconducting impedance-matching circuits, *Nat. Commun.* **6**, 7165 (2015).
- [32] David M. Pozar, *Microwave Engineering*, 3rd ed. (John Wiley & Sons Inc., New York, 2005).
- [33] Z. Chen and J. Appenzeller, in *Proceedings of the IEEE International Electron Devices Meeting 2008, Technical Digest* (IEEE, London, 2008), pp. 509–512.
- [34] Jilin Xia, Fang Chen, Jinghong Li, and Nongjian Tao, Measurement of the quantum capacitance of graphene, *Nat. Nanotechnol.* **4**, 505 (2009).
- [35] S. Dröscher, P. Roulleau, F. Molitor, P. Studerus, C. Stampfer, K. Ensslin, and T. Ihn, Quantum capacitance and density of states of graphene, *Appl. Phys. Lett.* **96**, 152104 (2010).
- [36] G. L. Yu, R. Jalil, Branson Belle, Alexander S. Mayorov, Peter Blake, Frederick Schedin, Sergey V. Morozov, Leonid A. Ponomarenko, F. Chiappini, S. Wiedmann, Uli Zeitler, Mikhail I. Katsnelson, A. K. Geim, Kostya S. Novoselov, and Daniel C. Elias, Interaction phenomena in graphene seen through quantum capacitance, *Proc. Natl. Acad. Sci. U.S.A.* **110**, 3282 (2013).
- [37] Jiamin Xue, Javier Sanchez-Yamagishi, Danny Bulmash, Philippe Jacquod, Aparna Deshpande, K. Watanabe, T. Taniguchi, Pablo Jarillo-Herrero, and Brian J. LeRoy, Scanning tunnelling microscopy and spectroscopy of ultra-flat graphene on hexagonal boron nitride, *Nat. Mater.* **10**, 282 (2011).
- [38] L. A. Ponomarenko, R. Yang, R. V. Gorbachev, P. Blake, A. S. Mayorov, K. S. Novoselov, M. I. Katsnelson, and A. K. Geim, Density of States and Zero Landau Level Probed through Capacitance of Graphene, *Phys. Rev. Lett.* **105**, 136801 (2010).
- [39] D. C. Elias, R. V. Gorbachev, A. S. Mayorov, S. V. Morozov, A. A. Zhukov, P. Blake, L. A. Ponomarenko, I. V. Grigorieva, K. S. Novoselov, F. Guinea, and A. K. Geim, Dirac cones reshaped by interaction effects in suspended graphene, *Nat. Phys.* **7**, 701 (2011).
- [40] Jungseok Chae, Suyong Jung, Andrea F. Young, Cory R. Dean, Lei Wang, Yuanda Gao, Kenji Watanabe, Takashi Taniguchi, James Hone, Kenneth L. Shepard, Phillip Kim, Nikolai B. Zhitenev, and Joseph A. Stroscio, Renormalization of the Graphene Dispersion Velocity Determined from Scanning Tunneling Spectroscopy, *Phys. Rev. Lett.* **109**, 116802 (2012).
- [41] Vadim V. Cheianov and Vladimir I. Fal'ko, Selective transmission of dirac electrons and ballistic magnetoresistance of n - p junctions in graphene, *Phys. Rev. B* **74**, 041403 (2006).
- [42] E. Pallecchi, A. C. Betz, J. Chaste, G. Fève, B. Huard, T. Kontos, J.-M. Berroir, and B. Plaçaïs, Transport scattering time probed through rf admittance of a graphene capacitor, *Phys. Rev. B* **83**, 125408 (2011).
- [43] Mojtaba Javaheri Rahim, Thomas Lehleiter, Daniel Bothner, Cornelius Krellner, Dieter Koelle, Reinhold Kleiner, Martin Dressel, and Marc Scheffler, Metallic coplanar resonators optimized for low-temperature measurements, *J. Phys. D* **49**, 395501 (2016).
- [44] Martin Gmitra, Denis Kochan, Petra Högl, and Jaroslav Fabian, Trivial and inverted dirac bands and the emergence of quantum spin Hall states in graphene on transition-metal dichalcogenides, *Phys. Rev. B* **93**, 155104 (2016).
- [45] G. L. Yu, R. V. Gorbachev, J. S. Tu, A. V. Kretinin, Y. Cao, R. Jalil, F. Withers, L. A. Ponomarenko, B. A. Piot, M. Potemski, D. C. Elias, X. Chen, K. Watanabe, T. Taniguchi, I. V. Grigorieva, K. S. Novoselov, V. I. Fal'ko, A. K. Geim, and A. Mishchenko, Hierarchy of Hofstadter states and replica quantum Hall ferromagnetism in graphene superlattices, *Nat. Phys.* **10**, 525 (2014).